INL/JOU-17-44244-Revision-0

Rechargeable Li metal battery cell design and the role of lean electrolyte on cycle life

Shrikant C. Nagpure, Tanvir R. Tanim,
Eric J. Dufek, Vilanuyur V. Viswanathan,
Alasdair J. Crawford, Sean M. Wood, Jie
Xiao, Charles C. Dickerson, Boryann Liaw

October 2018

INL/JOU-17-44244-Revision-0

Rechargeable Li metal battery cell design and the role of lean electrolyte on cycle life

Shrikant C. Nagpure, Tanvir R. Tanim, Eric J. Dufek, Vilanuyur V. Viswanathan, Alasdair J. Crawford, Sean M. Wood, Jie Xiao, Charles C. Dickerson, Boryann Liaw

October 2018

Idaho National Laboratory
Idaho Falls, Idaho 83415

http://www.inl.gov

Prepared for the
U.S. Department of Energy
Office of Energy Efficiency and Renewable Energy
Under DOE Idaho Operations Office
Contract Unknown

Impacts of lean electrolyte on cycle life for rechargeable Li metal batteries

Shrikant C. Nagpure[1,#], Tanvir R. Tanim[1,#], Eric J. Dufek[1,*], Vilayanur V. Viswanathan[2], Alasdair J. Crawford[2], Sean M. Wood[1], Jie Xiao[2], Charles C. Dickerson[1], and Boryann Liaw[1]

[1]Energy Storage and Advanced Vehicles Department, Idaho National Laboratory, Idaho Falls, ID 83415
[2] Electrochemical Materials and Systems Group, Pacific Northwest National Laboratory 99352

Abstract

Strong demand for higher energy batteries for extended range electric vehicles has driven battery technology development toward Li metal batteries. One limitation of Li metal batteries is cycle life. At odds are the amount of electrolyte to fulfill high energy and the amount needed to achieve long cycle life. Here we employ an electrochemical model and design of experiment to understand impacts on cycle life and failure as electrolyte content is reduced to levels needed to achieve reasonably high specific energy. With lean electrolyte, a gap exists in achieving long cycle life with a reduction by a factor of 6.5 when electrolyte amount is reduced from 37.0 g Ah^{-1} to 6.0 g Ah^{-1}. Two primary failure routes are identified with differences between lean and high electrolyte quantities. The results suggest that reporting and performing experiments for high energy cell designs requires that amount of electrolyte be considered a critical parameter.

Keywords: Lithium metal, electrolyte, high specific energy, cycle life, battery

[#]Equal first authors

[*]*Corresponding author: Tel.: +1 208 526 2132; fax: +1 208 526 8541. Email address:* *eric.dufek@inl.gov (E.J. Dufek)*

Acronyms

LIB	lithium-ion battery
RLB	rechargeable Li metal battery
NMC622	$LiNi_{0.6}Mn_{0.2}Co_{0.2}O_2$
SPM	single particle model
EC	ethylene carbonate
EMC	ethylmethyl carbonate
PVDF	polyvinylidene fluoride
PET	polyethylene terephthalate
PP	polypropylene
DS	dual salt
LiBOB	lithium bis(oxalato)borate
LiTFSI	lithium bis(trifluoromethanesulfonyl)imide
$LiPF_6$	lithium hexafluorophosphate
RPT	reference performance test
RSD	relative standard deviation
CE	coulombic efficiency
CC	constant current
CV	constant voltage
$dQ\ dV^{-1}$	differential capacity

1.Introduction

Li-ion battery (LIB) technology has enabled widespread use of portable and wearable consumer electronics and an increased adoption of electric vehicles. As specific energy and cycle life improve, the overall cost of LIBs has also significantly reduced [1]. Demands for higher energy and power cell designs are driving current battery technology developments. However, there are theoretical limitations on the maximum specific energy and energy density that can be achieved with LIBs. Several routes to achieving higher specific energy in rechargeable Li metal batteries (RLBs) are being considered [2]. Shifting to Li metal, which has high theoretical specific capacity of 3,860 mAh g^{-1} and a negative reduction potential of −3.05 V vs a normal hydrogen electrode, provide the possibility to design batteries that exceed the limitations of LIBs. One specific RLB design is the use of a Li metal negative electrode, a liquid electrolyte and a nickel-rich oxide material such as $LiNi_{0.6}Mn_{0.2}Co_{0.2}O_2$ (NMC622) [3,4]. These cells have the ability to readily exceed 300 Wh kg^{-1}.

While capable of achieving high specific energies, RLBs suffer from low cycle life which can be attributed to the degradation of the Li electrode [5]. Indeed, a significant focal point of RLB research has been on improving the cyclability of Li using different protection schemes including organic and inorganic coatings, [6–10] and electrolytes [9–14]. Although advancements have been made at improving cycle life, the overall focus for most experimental efforts to improve Li cycling efficiency and cycle life do not take into account the overall balance of materials required to construct a RLB that is competitive on a Wh kg^{-1} basis with current state-of-the-art LIBs which are approaching 300 Wh kg^{-1} [15].

To enable cells with a high specific energy, cell components must be optimized to translate the benefits of high energy materials. This is true even when using a Li metal negative electrode.

Specifically, when accounting for the complete cell design, little flexibility remains to reduce cell mass through the reduction of inactive, non-electrolyte components. Instead, to exceed 300 Wh kg^{-1}, it is necessary to precisely control key components such as the quantity of the NMC622 material, the electrolyte and the thickness of Li used. Here, a combined approach is used to understand how cycle life for RLBs is impacted by the use of lean electrolyte conditions that are necessary for a cell to approach and exceed 300 Wh kg^{-1}. Analysis is performed using a joint design of experiments that is closely coupled to a single particle modeling (SPM) approach to define electrolyte quantities necessary for high specific energy design. Observed declines in performance with reduced electrolyte highlight the distinct need to closely coordinate experimental conditions with design parameters needed to achieve high specific energy with RLBs.

2.Experimental

2.1 Electrochemical Model

An electrochemical, SPM was used to identify appropriate electrolyte amounts for reasonably high energy RLB cells and to aid in the design of experiments. Analysis considered a pouch cell design with stacked electrodes shown in Fig. 1a. Cell specific energy was calculated using Eq. (1) where m is the mass and the subscript corresponds to different cell components. To aid in the design of experiments with respect to electrolyte quantity, the non-electrolyte design parameters (listed in Table 1) were held constant.

$$\text{Specific energy} = \frac{\text{Available energy}}{\left(m_{\text{NMC}} + m_{\text{binder}} + m_{\text{filler}} + m_{\text{Li}} + m_{\text{elec}} + m_{\text{cu}} + m_{\text{al}} + m_{\text{sep}} + m_{\text{tab}} + m_{\text{pouch}}\right)} \tag{1}$$

The SPM approach [16,17] was used to simulate the voltage response of the NMC-based RLB and to more reliably evaluate the specific energy of cell designs. The SPM solved the solid phase diffusion equations for a single particle in the positive electrode assuming uniform current density distribution. This approach has been shown to perform well for low and moderate C-rates for LIB applications [17]. To align the SPM with the RLB cell design, the conventional graphite electrode in a LIB was replaced by the planar, solid Li metal electrode.

Available energy is typically measured at relatively low C-rates (e.g., C/3) [16,17], providing good applicability of the SPM model for design of RLBs. For the present work, the open circuit potential for the positive electrode was approximated using a C/20 constant current discharge in a CR2032 coin cell (Fig. 1b). The open circuit potential of the Li electrode was considered to be at 0V vs Li/Li^+. Other model input parameters are provided in Table 1.

Table 1: Design and input parameters of a 2.18 Ah cell

Material	Property Value	Design parameter	Value
Li (g cm^{-3})	0.534	Specific capacity (mAh g^{-1})	198
NMC622 (g cm^{-3})	4.7	NMC622 active mass fraction (%)	90
Electrolyte density(g cm^{-3})	1.19	Binder (PVDF) fraction (%)	5
PVDF (g cm^{-3})	1.75	Carbon filler fraction (%)	5
PET (g cm^{-3})	2.2	Single side positive electrode thickness (μm)	59.5
Carbon filler (g cm^{-3})	0.946	Separator thickness (μm)	25
Polypropylene (g cm^{-3})	1.4	Separator porosity (%)	55
Al (g cm^{-3})	2.7	Excess Li (%)	100
Cu (g cm^{-3})	8.96	Cell height (cm)	6.1
		Cell area (cm^{2})	19.4
		Al foil thickness (μm)	15
		Cu foil thickness (μm)	10
		Packing foil thickness (μm)	
		PET	60
		PP	50
		Tab mass	
		Major (g tab^{-1})	0.057
		Minor (g layer^{-1})	0.024

Other modeling inputs	Value
Temperature (°C)	25
Maximum voltage (V)	4.4
Minimum voltage (V)	2.8
Particle radius (μm)	4.5
Stoichiometry, θ	
θ_{max}	1.0
θ_{min}	0.32
Max conc. of Li in NMC (mol cm^{-3}) [16]	0.05330
Positive electrode exchange current density (A cm^{-2})[16,19]	1.97×10^{-4}
Negative electrode exchange current density (A cm^{-2})[18,20]	3.16×10^{-2}
Charge transfer coefficients [19]	0.5
Positive electrode particle diff. coefficient (cm^{2} s^{-1}) [21]	5×10^{-11}
Li-ion Electrolyte diffusion coefficient (cm^{2} s^{-1}) [23]	3.35×10^{-6}
Electrolyte conductivity (S cm^{-1}) [22]	8.3×10^{-3}
Salt concentration (mol cm^{-3}) [20]	1.15
Li transference number [16,22]	0.38
Bruggemann's exponent [19,23]	
Positive electrode	1.35
Separator	1.5

For SPM calculations the cell capacity was maintained near 2 Ah and kept constant by varying the total electrode area and the number of unit cells (stacks) within the cell (Fig. 1a). The total capacity of the cell was dictated by the capacity of the NMC positive electrode. One hundred percent excess Li, based on the Li mass in the positive electrode, was used to define the negative electrode thickness. Thus the total Li in the negative electrode was equal to two times the Li in the positive electrode. The total number of electrodes dictates the number of current collectors and minor tabs required. With known numbers of unit cells, the cell thickness was calculated using Eq. (2) to estimate packing foil mass. Here L_p and L_n correspond to the thicknesses of the positive and negative electrodes respectively, L_{sep} is the separator thickness, and L_{Cu} and L_{Al} are the thickness values for the Cu and Al current collectors, respectively.

$$\text{Cell thickness} = \text{\# units cells} \times \left(\mathrm{L_p} + \mathrm{L_{sep}} + \mathrm{L_n} + \frac{\mathrm{L_{Cu}}}{2} + \frac{\mathrm{L_{Al}}}{2}\right) + \frac{\mathrm{L_{Cu}}}{2} + \frac{\mathrm{L_{Al}}}{2} \tag{2}$$

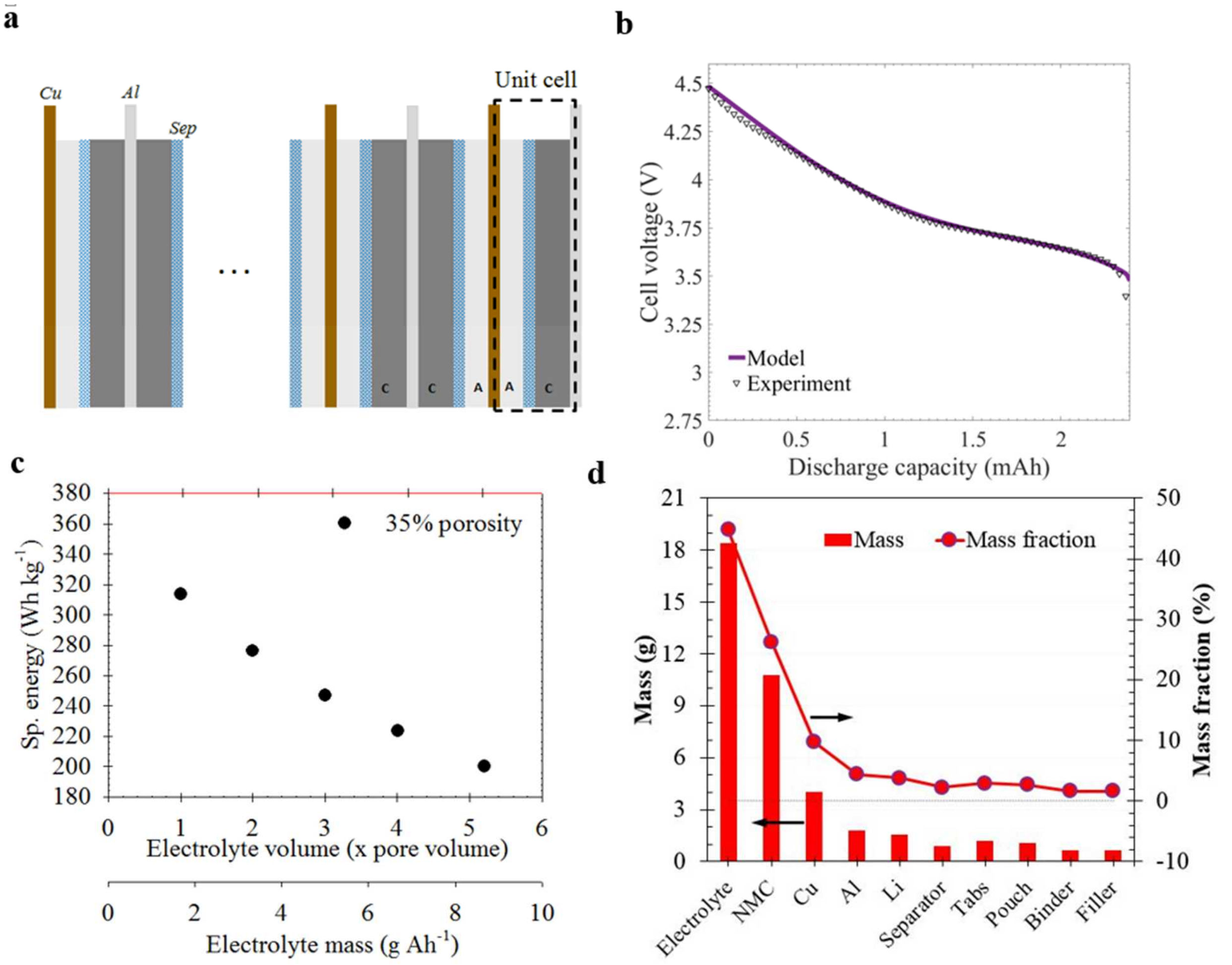

Fig 1: Cell design and modeling approach: (a) stacked electrode design where C corresponds with the positive electrode and A denotes the negative electrode, (b) C/20 cell voltage comparison for experimental and model data for Li || NMC622 where the cathode is 35% porous, (c) specific energy as a function of electrolyte volume or mass (d) masses of cell components with 420% excess electrolyte (5.2×pore volume).

The effect of varying the quantity of electrolyte on the specific energy for a cell with a 35% porous positive electrode, is shown in Fig. 1c. This porosity corresponds to the electrode laminate used in the experimental work. In the x-axis of Fig. 1c the electrolyte volume is plotted as a multiple of the cell pore volume which includes the pore volumes from the positive electrode and separator [15]. For instance, electrolyte equal to 1x pore volume indicates no excess and 5.2x pore volume suggests a 420% excess electrolyte condition. The respective mass of cell components for 420% excess electrolyte are shown in Fig. 1d. Table 2 provides comparable electrolyte volumes when scaled to a coin cell using the experimental NMC622 electrode. Equivalent electrolyte amounts in terms of g Ah^{-1}, calculated using the as prepared positive electrode loadings and the respective electrolyte mass, have also been included in Fig. 1 and Table 2.

The electrodes used for the experiment varied from the SPM calculations in Fig. 1 in that the electrode used for experiments has a lower loading of 1.45 mAh cm^{-2} compared to 2.53 mAh cm^{-2} in Fig. 1. The main impact of this reduced loading of NMC622 is that the current density at the Li metal electrode during charging and discharging is altered as the capacity of the positive electrode increases. Understanding current density limitations on cycle life is important here, as acceptable rates which can be used to minimize rapid loss of capacity vary by at least an order of magnitude for different electrolytes [12,24,25]. For the present evaluation, the current densities for different experimental conditions fall well below the previously reported range where minimal capacity fade is observed (1.75 mA cm^{-2}) [12].

Table 2: Electrolyte and current density parameters

Electrolyte quantity		
µL	***g Ah^{-1}***	***% Pore Volume***
12	6.0	245
20	10.2	409
24	12.0	491
75	37.0	1533
Geometric current densities at Li (mA cm^{-2})		
Rate		*Experimental*
C/3		0.48
C/10		0.14
C/20		0.07

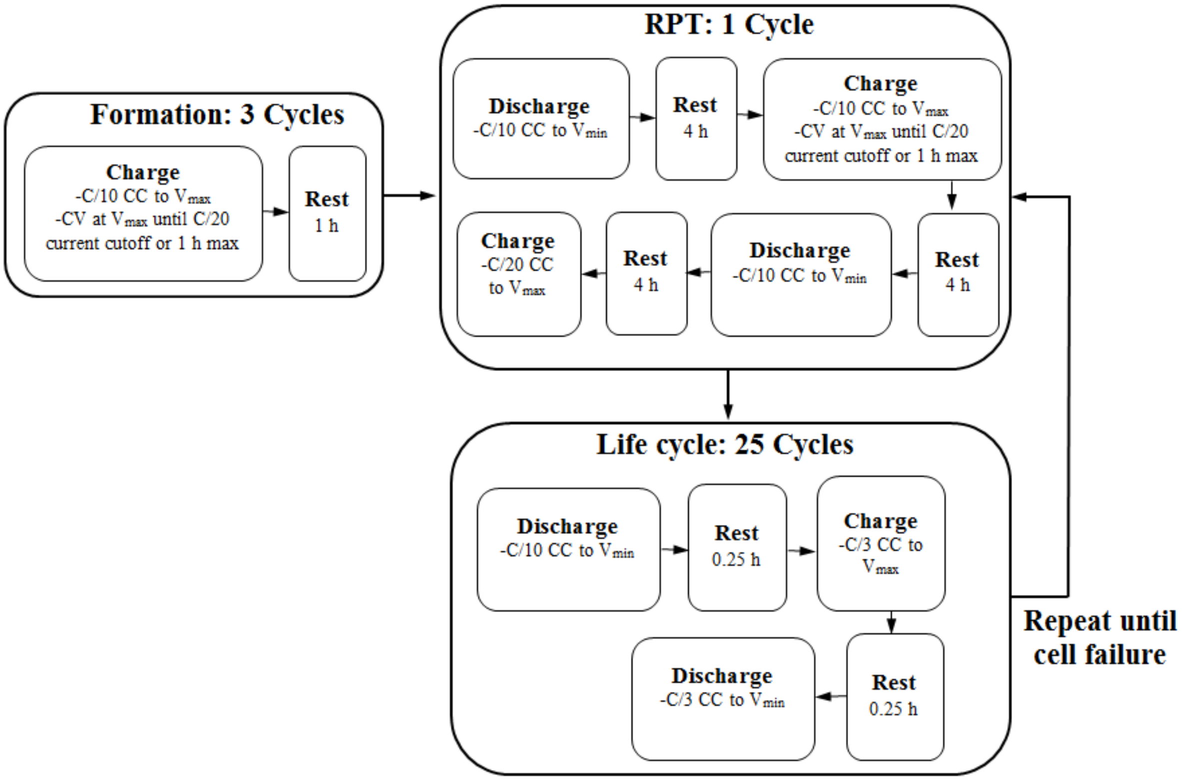

Figure 2: Electrochemical performance evaluation tests

2.2 Electrolyte and cell preparation

Modified dual salt electrolyte blends [12] were prepared by combination of ethylene carbonate (EC, BASF), ethyl methyl carbonate (EMC, BASF), vinylene carbonate (VC, BASF), lithium bis(oxalato)borate (LiBOB, BASF), lithium bis(trifluoromethanesulfonyl)imide (LiTFSI, BASF) and lithium hexafluorphosphate ($LiPF_6$, Kishida). The final electrolyte composition was 3:7 (w/w) EC: EMC with 0.6M LiTFSI, 0.4M LiBOB, 50 mM $LiPF_6$ and 2 wt% VC. The dual salt electrolyte has previously been shown to enable a relatively high cycle life for Li || NMC442 systems [12,13]. The present work slightly modified the previous dual salt electrolyte with an additional 2% VC to aid solid electrolyte interphase formation and stability. Electrolyte conductivity was determined using a TOA CM-30R conductivity meter. A Cambridge DL-4100 (falling bob) viscometer was used for viscosity measurements. Both viscosity and conductivity measurements were performed at room temperature (20°C) and at least seven measurements were averaged to obtain the values reported.

Full CR-2032 Li || NMC622 coin-type cells were assembled in an Ar-filled glovebox with H_2O and O_2 levels below 0.2 ppm using the electrolyte volumes shown in Table 2. The coin cells were prepared with metallic Li foil negative electrode (1.43 cm diameter, 250 μm thick, MTI) in direct contact with a stainless steel spacer (1.43 cm diameter, 0.5 mm thick) which rested on a spring. For the positive electrode a blend of 90% NMC622 with 5% Timcal C45 carbon black and 5% polyvinylidene fluoride (PVDF) binder was used. Positive electrode laminates were provided by the Cell Analysis, Modeling and Prototyping facility at Argonne National Laboratory. The punched positive electrodes also had a diameter of 1.43 cm and a total loading of 10.03 mg cm^{-2} (without foil, but including inactive components) and were cast on 20 μm thick Al foil. The total electrode thickness was 58 μm (1.45 mAh cm^{-2} loaded capacity) with a calendared porosity of

35.5% (based on loading and final thickness following electrode calendaring). The positive electrode was also in direct contact with a stainless steel spacer. Celgard 2500 (1.53 cm diameter) was used as the separator. Non-Li cell components were dried at 60°C (at vacuum strength greater than -75 kPa) for a minimum of 8 h prior to introduction into the glovebox for cell fabrication.

2.3 Electrochemical performance evaluation and analysis

Cell testing was performed in triplicate for each condition. Specific capacity for each cell was determined based on the respective mass of each positive electrode. Cells were cycled between a minimum voltage (V_{min}) of 2.8 V and a maximum voltage (V_{max}) of 4.4 V. For each electrolyte amount, the data shown corresponds to the highest performing cell (longest cycle life) for each electrolyte quantity. Prior to initiating testing using a calibrated Maccor 2000 series battery tester, cells were allowed to equilibrate for 2 h in an environmental chamber (ESPEC BTU 133) at 25˚C. During testing, the cells were maintained at 25±3˚C. The cycling protocol for the cells is shown in Fig. 2. The test protocol can be generally broken down into three regimes: formation at the beginning of life, a reference performance test (RPT) which consisted of two cycles (one at C/10 and one at C/20), and a cycle life aging regime. The total cycle count includes cycle numbers from all three test regimes (i.e., formation, RPT and cycle life counts).

3.1 Results

3.1.1 Cell Design to Inform Design of Experiments

When considering high specific energy cells, understanding cell design limitations significantly aids the design of experiments. One area specifically restricted by design limitations is the quantity of electrolyte used. As an example, for the present Li‖NMC622 cell, the use of between 4.0 and 6.0 g Ah^{-1} of electrolyte results in a cell with specific energy that is on par with many state-of-the art commercial Li-ion cell designs (Fig. 1). These electrolyte quantities are significantly below what are typically used for many Li metal, coin cell studies reported in the open literature which usually use in excess of 75 μL [26]. Using the guidance from Fig. 1 an experiment was designed to better understand the failure mode impacts as a function of electrolyte quantity (Table 2).

3.1.2 Impact of lean electrolyte on cycle life

Using the conditions identified in Table 2, cells were cycled to more directly understand failure mode variation. To gauge performance degradation and failure, RPTs were performed at the beginning of cycling and after every 25 cycles (Fig. 2). At the beginning of testing immediately following formation (defined as RPT0), regardless of electrolyte quantity the initial discharge specific capacity, based on NMC622 loading, had high uniformity with a range from 198-200 mAh g^{-1} at C/20 (Fig. 3). The data, when adjusting for the V_{max} of 4.4 V, is in line with reported values for NMC622 [4]. The variability across each set of cells was also low during initial cycling. As the cells aged, increased variation in the rate of fade and a shortened cycle life occurred as lower quantities of electrolyte were used. The spread in variation can be readily compared by tracking the relative standard deviation (RSD) for each electrolyte quantity between the first C/3 cycle following RPT0 to the 25th C/3 cycle which immediately preceded RPT1. The RSD was determined by taking the standard deviation of the cells (in mAh g^{-1}), dividing by the average specific capacity for each of the four electrolyte conditions at a specific cycle number and then converting the value to a percentage. For the 1st C/3 cycle the RSD across the four electrolyte conditions (shown in parenthesis) were 2.8% (6.0 g Ah^{-1}), 4.4% (10.2 g Ah^{-1}), 0.5% (12.0 g Ah^{-1}) and 0.8% (37.0 g Ah^{-1}). By the 25th C/3 cycle, RSD for each condition had respectively shifted to 17%, 9.5%, 0.9% and 0.5% indicating growing variability as a function of cycling for the lean electrolyte conditions (6.0 and 10.2 g Ah^{-1}). While more complete analysis of the variability is needed, for the present work a comparison of the top performers (longest cycle life) for each electrolyte quantity was performed.

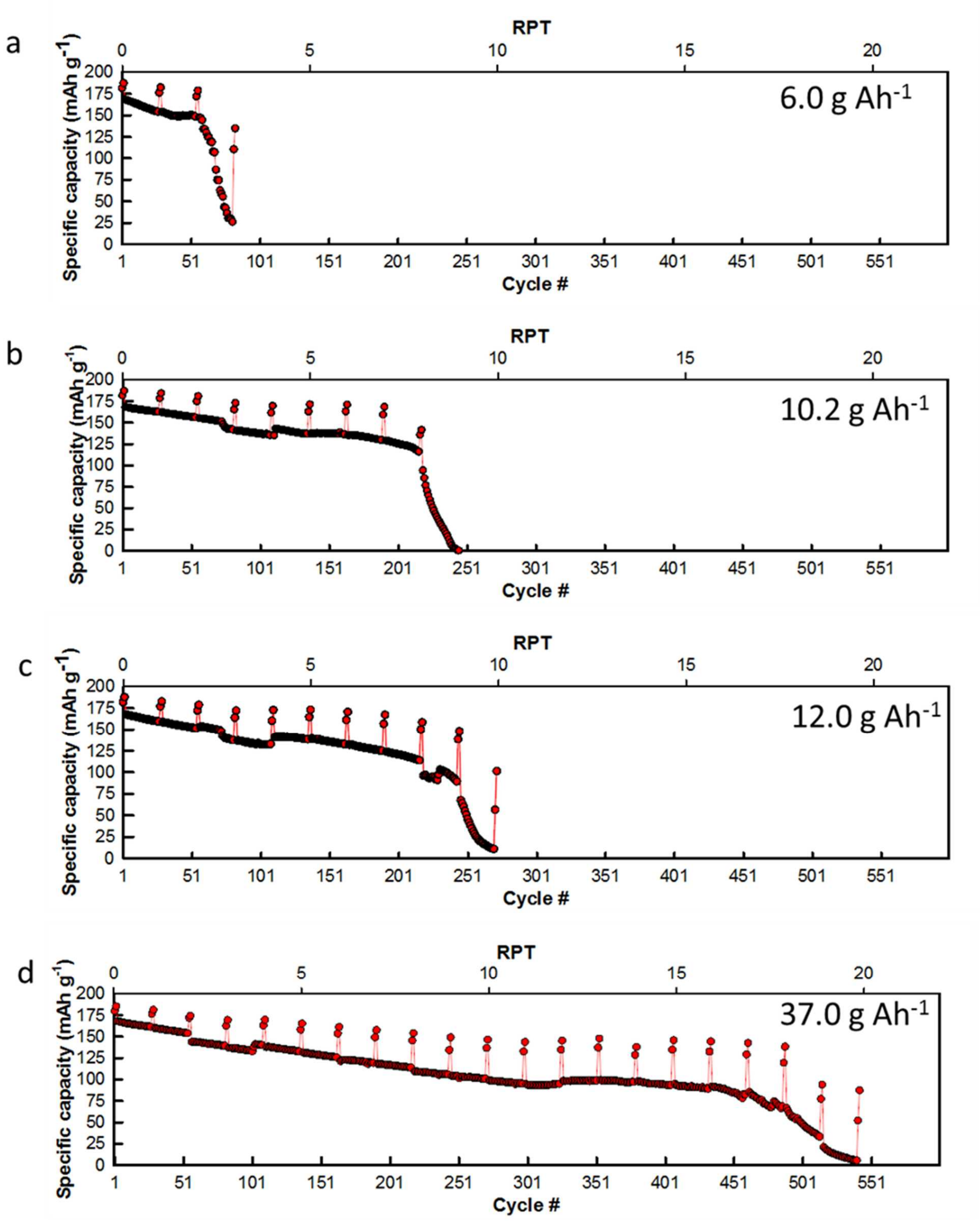

Figure 3: Discharge specific capacity (based on NMC622 active material loading) as a function of cycle number (bottom x-axis) and RPT (top x-axis) for the four different electrolyte quantities a) 6.0 g Ah^{-1}, b) 10.2 g Ah^{-1}, c) 12.0 g Ah^{-1}, and d) 37.0 g Ah^{-1}.

For each electrolyte condition a linear capacity fade was observed during initial cycling. The cells with electrolyte quantities greater than 10 g Ah^{-1} of electrolyte displayed fade rates between 0.24 and 0.32 mAh g^{-1} cycle^{-1} while the lean condition (6.0 g Ah^{-1}) faded at nearly two times faster at >0.50 mAh g^{-1} cycle^{-1}. Extending the analysis for the entire life of the cells using the data in Fig. 4 shows overall fade rates do not vary significantly for the high electrolyte quantities. However a considerable increase occurs for the lean electrolyte condition of 6.0 g Ah^{-1} lean to over 1.2 mAh g^{-1} cycle^{-1}. The distinct difference in fade between low and high electrolyte quantities suggests different failure routes.

The coulombic efficiency (CE) for each of the conditions was also highly uniform during early cycling. For each conditions through the first three RPTs, the CE was maintained in excess of 99.6% (data not shown). Only as the cells began to fail did the CE start to fall significantly below 99%. However, given that the cells were constructed with excess Li, the CE values are skewed by the ability to readily access the reservoir of excess Li. This ability to extract additional Li artificially increases CE of the cells, and as such it was not used as a major metric of performance.

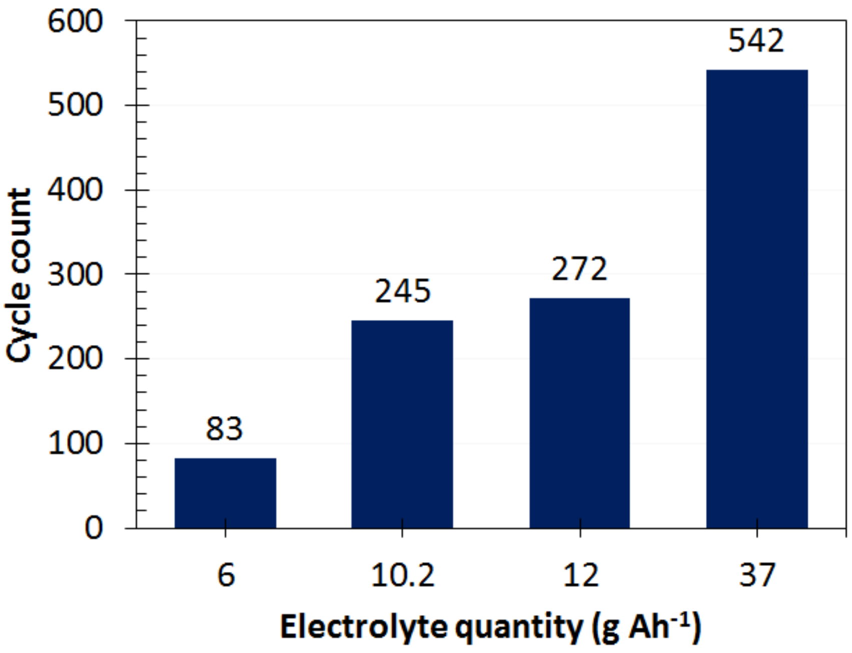

Figure 4: Cycle life of cells as a function of electrolyte content (in g Ah^{-1}*) to illustrate the impact of electrolyte quantity on cycle aging.*

The charge and discharge profiles at multiple RPTs are shown in Figure 5 (C/3) and Figure 6 (C/20) for each of the electrolyte quantities. In Fig. 5 similar capacities are observed across the cells, but the knee for the 6.0 mAh g^{-1} condition is more gradual. As aging occurs, differences between the C/3 and C/20 capacities indicate emerging kinetic limitations which vary as a function of electrolyte quantity.

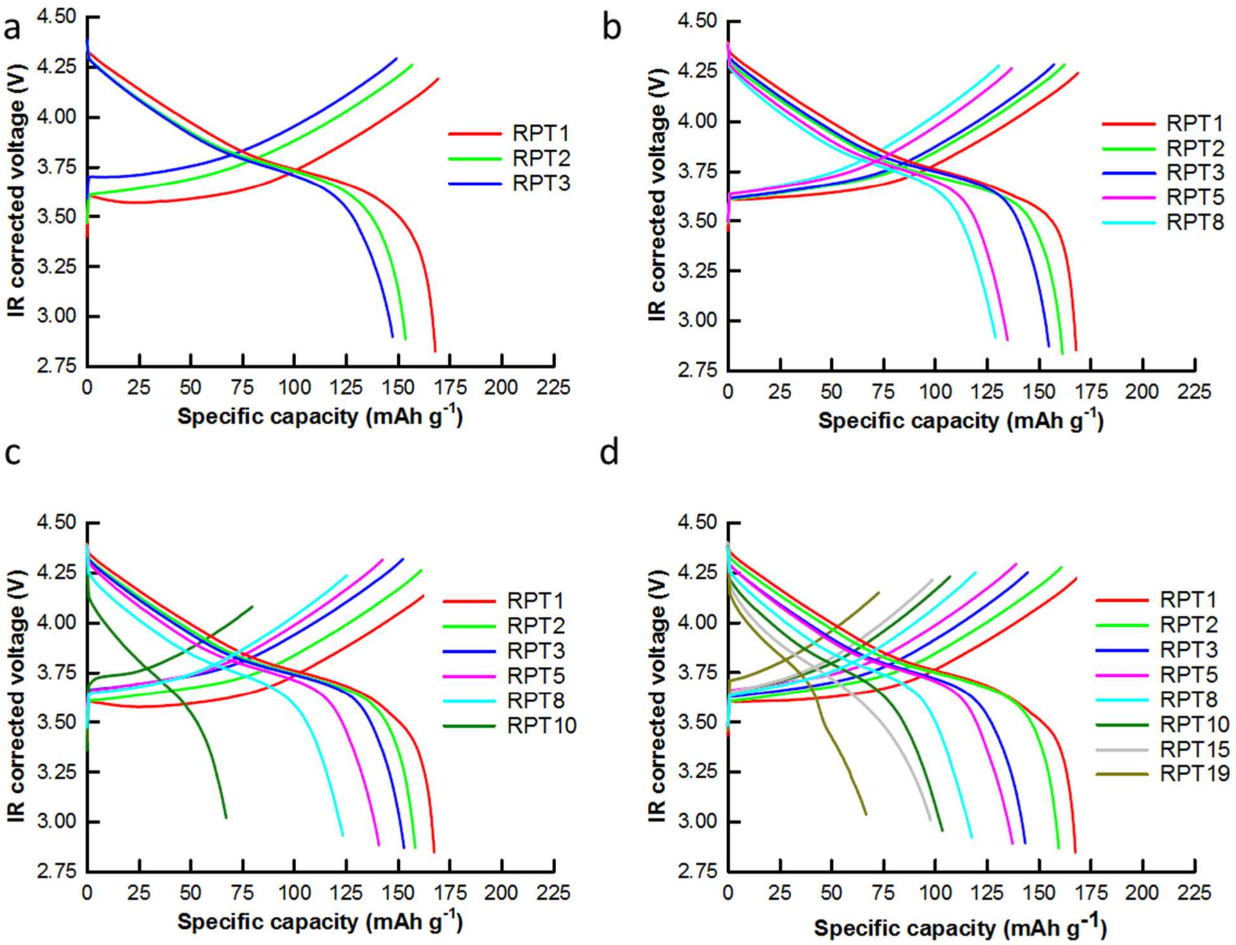

Figure 5: C/3 charge and discharge profiles for the four different electrolyte quantities a) 6.0 g Ah^{-1} b) 10.2 g Ah^{-1}c) 12.0 g Ah^{-1}d) 37.0 g Ah^{-1}. Note that the C/3 profiles correspond to the last C/3 cycle just prior to the reported RPT number.

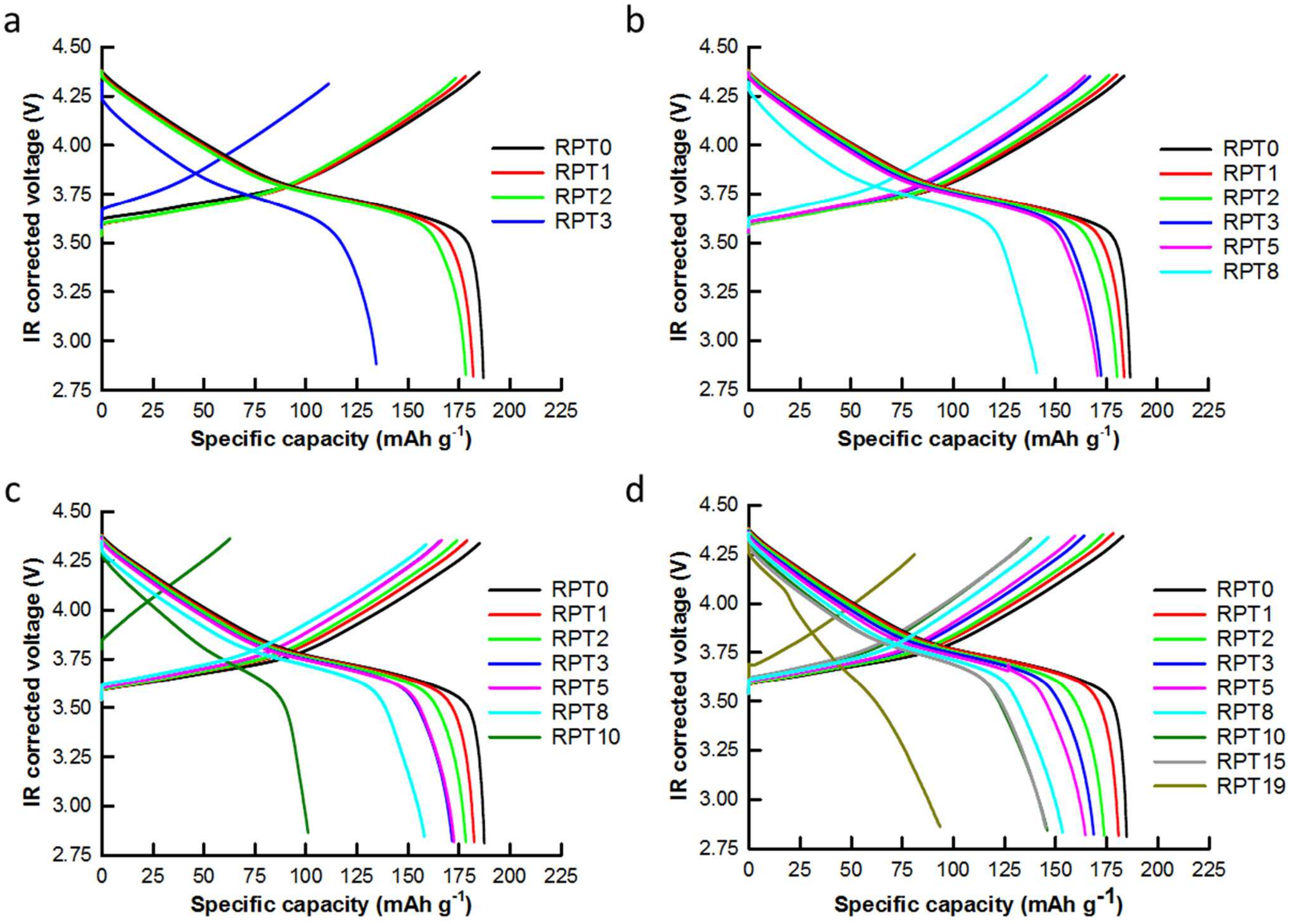

Figure 6: C/20 charge and discharge profiles as a function of age for the four different electrolyte conditions a) 6.0 g Ah^{-1}, b) 10.2 g Ah^{-1}, c) 12.0 g Ah^{-1}, and d) 37.0 g Ah^{-1}

Figs. 3-6 clearly show performance difference as electrolyte quantity is varied. Additional analysis using differential methods such as differential capacity analysis (dQ dV^{-1}) provides the opportunity to understand failure modes [27–29]. Figure 7 provides information which begins to explain the evolution of failure for the Li || NMC622 system as the electrolyte quantity is reduced. During initial charging, each of the four electrolyte conditions displayed the same behavior: well-defined peaks associated with Ni-redox within the NMC622 followed by a plateau which corresponds to the higher voltage solid solution of the NMC [4]. For each condition the slight, negative-going peak at the beginning of the charge cycle near 3.55 V for RPT0 likely corresponds to the overpotential for Li deposition. This overpotential includes components associated with electrolyte transport, charge transfer kinetics, and Li nucleation [30,31].

Through RPT2 small variations were seen in the dQ dV^{-1} plots; the most profound variation being a slightly enhanced reduction in the intensity of the peak centered near 3.75 V. Only as the cell with 6.0 g Ah^{-1} of electrolyte approached failure was there an observed change in the lower voltage charging peaks. For the 6.0 g Ah^{-1} condition, the solid solution region on the charging dQ dV^{-1} saw no significant alteration, even after significant capacity loss. This indicates the positive electrode material had negligible fade. For the higher electrolyte quantity cells, as the cycling advanced beyond RPT5, the charging voltage and negative-going peak from Li deposition shifted to higher values and the slope of the peak near 3.7 V became less steep. As with the low electrolyte quantities, little change was observed in the higher voltage solid solution region of the NMC622.

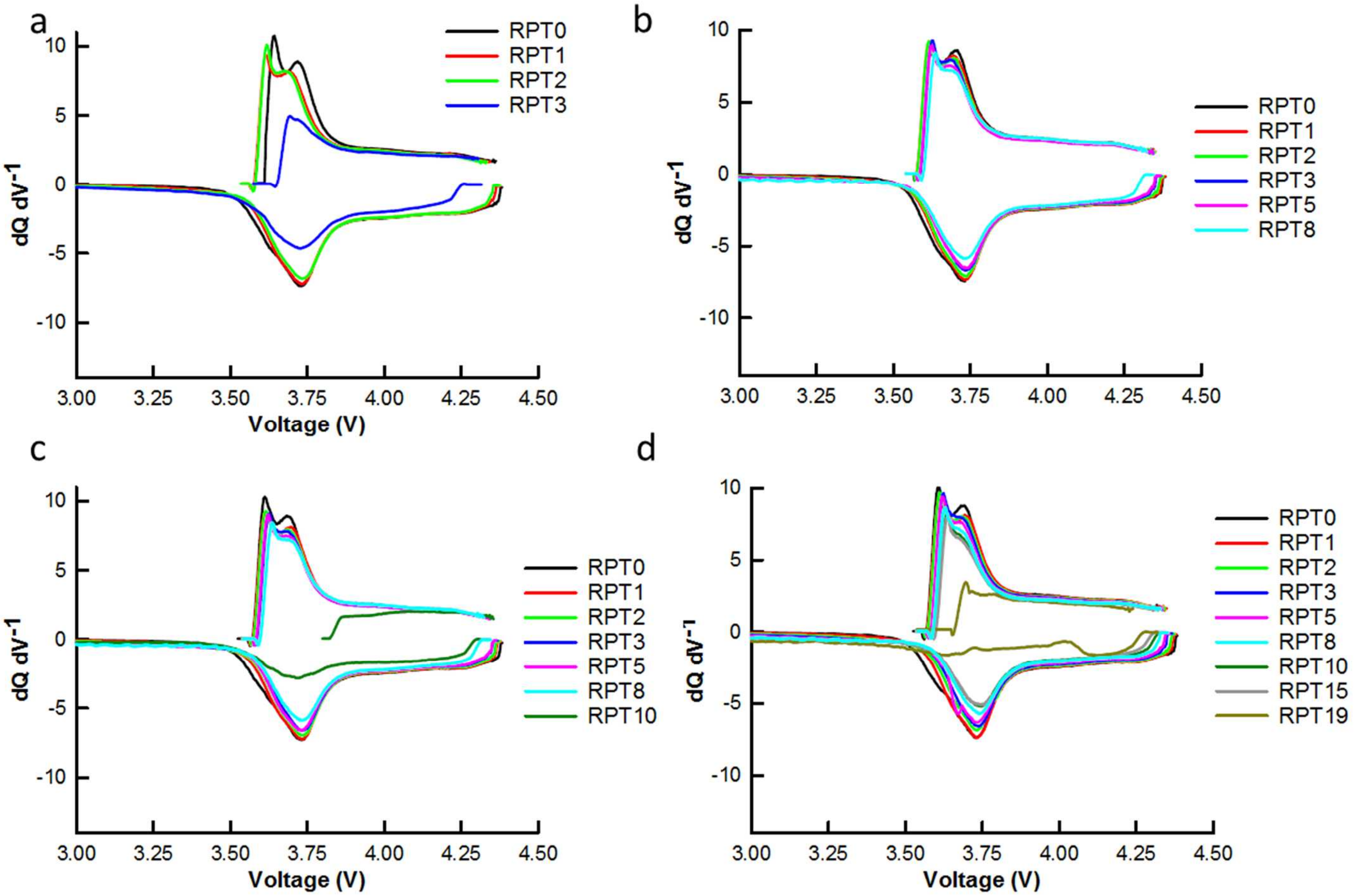

Figure 7: dQ dV^{-1} plots for data collected at C/20 during the RPTs for the different electrolyte conditions as a function of aging for the four different electrolyte quantities a) 6.0 g Ah^{-1}, b) 10.2 g Ah^{-1},c) 12.0 g Ah^{-1} , and d) 37.0 g Ah^{-1}. Positive values on the y-axis correspond to the charging behavior while negative values reflect the discharge.

As the cells aged, increased cell impedance led to a shift to lower voltages in the initial discharge portion of the dQ dV^{-1} plots. Additionally, the initial voltage at the beginning of the discharge gradually progressed to lower values. This occurred even when accounting for the increased impedance and indicates the extent of delithiation in the positive electrode altered as the cells aged. The extent of incomplete delithiation was exacerbated as less electrolyte was used. While the rate of delithiation varied with electrolyte quantity, in all cases the eventual cell failure was preceded by an abrupt loss in positive electrode utilization. For the 10.2 g Ah^{-1} condition this shift in delithiation extent occurred one RPT prior to failure while at 12.0 g Ah^{-1} the shift was two RPTs prior to failure. As with the charging side of the dQ dV^{-1} plot, as the cells aged the intensity of the primary discharge peak at 3.76 V reduced suggesting that over time the lithiation state of the positive electrode was decreasing.

For all electrolyte conditions, the dQ dV^{-1} data indicate a shift in the onset of the charge and discharge processes, but little overall shift in the position of the electrochemical processes as the cells age. Previous reports suggest this behavior is likely caused by an increased cell impedance [4], though in the present case the increased impedance has little true impact on the bulk of the processes while evaluating the cells at a C/20 rate during the RPT. To better judge kinetic effects, it is necessary to look at performance at different rates. Figure 8 compares the ratio of the charge and discharge capacity for the C/3 and C/20 cycling as a function of RPT. For this comparison, the C/20 capacity from the RPT was used, while the C/3 data corresponds to the first C/3 cycle after the RPT. The ratio of the two highlights the interplay between kinetic and material loss during aging. Lower ratios indicate active material is being less fully utilized at the C/3 rate due to the overall shift in cell kinetics. The shift in kinetics is mainly associated with impedance growth and transport issues as Li morphology evolves.

At the beginning of cycling, each of the electrolyte conditions attained a C/3:C/20 discharge capacity ratio of 0.9, which is lower than has previously been reported for sub-C/1 rate capability for NMC622 [4]. At the beginning of life, the greater rate disparity, when compared to previous reports is likely due to two factors. First, ionic conductivity of Li^+ in the electrolyte for the dual salt electrolyte is lower than previously reported values using $LiPF_6$-based electrolytes. For reference, blends of electrolyte using EC, EMC, or diethylene carbonate and 1.0 to 1.2 M

$LiPF_6$ typically have conductivities between 0.8 and 0.95 S m^{-1} and viscosities close to 4 cP [32–34], these values are well above the measured conductivity (0.635 ± 0.002 S m^{-1}) and below the measured viscosity (4.65 ± 0.4 cP) of the dual salt electrolyte. Secondly, the present cells had higher loading of NMC622 on the positive electrode which led to decreased rate performance (also exacerbated by diminished electrolyte ionic transport).

As the cells aged, the C/3 capacity dropped more rapidly than the C/20 capacity (Fig. 8). With the exception of the 6.0 g Ah^{-1} condition, the other three electrolyte conditions had similar rates of change for the C/3:C/20 ratio from RPT 0 to RPT 2 indicating each condition was experiencing similar rates of materials losses and decreased kinetics. For the lean electrolyte condition, the C/3:C/20 ratio had a more distinct decrease between RPT0 and RPT1 indicating the early emergence of kinetic issues. The shift to lower C/3:C/20 ratios highlights that while the overall active material available for cycling was not decreasing, transport within each condition significantly limited material utilization.

The rapid drop in capacity (Fig.3) during failure for the 6.0 and 10.2 g Ah^{-1} without corresponding drop in C/3: C/20 ratio (Fig. 8) prior to failure suggest a relatively rapid transition within the cell. This is due to a distinct evolution in the electrolyte composition as certain components are consumed during the repeated solid electrolyte interphase formation. For the higher electrolyte quantity conditions the increasingly worse rate performance suggests more gradual processes occur. The ultimate failure for the high electrolyte conditions, likely involves both Li^+ transport in the electrolyte as well as the formation of a more complex morphology of the Li metal electrode.

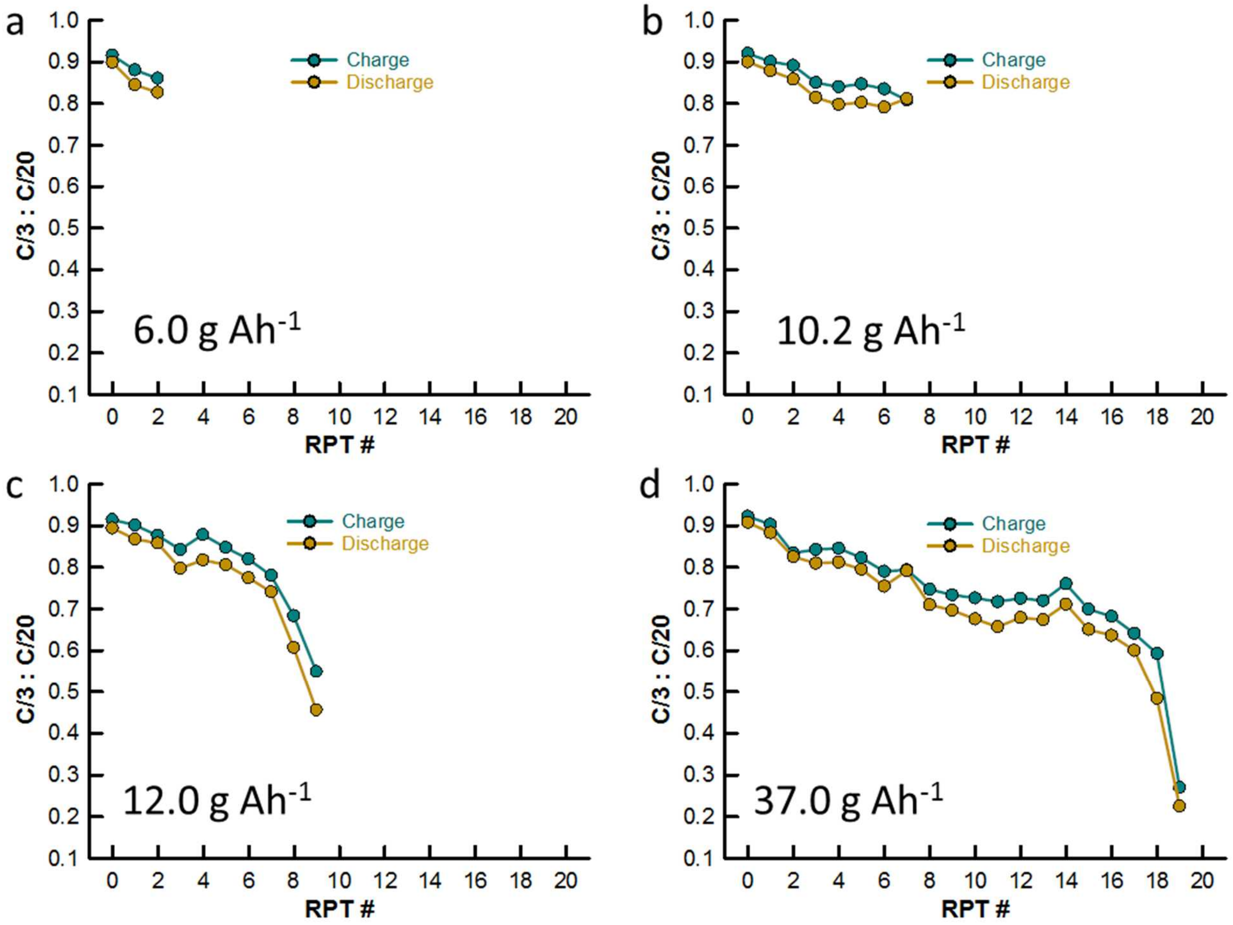

Figure 8: Ratio of the C/3 and C/20 charge and discharge capacities for the four different electrolyte quantities a) 6.0 g Ah^{-1}, b) 10.2 g Ah^{-1}, c) 12.0 g Ah^{-1}, and d) 37.0 g Ah^{-1}.

3.2 Discussion

To advance RLB technology, especially in cells over 1 Ah, it is necessary to directly link experimental assessment with reasonable cell designs. In the data shown above, clear variation in performance indicates that using flooded conditions in experimental work skews the results of experiment by over reporting performance to be expected in a realistic cell. The use of excess electrolyte also alters the means by which cells fail. Thus, to provide the most direct path forward for material and technology advancement it seems appropriate to perform a robust experiment design using conditions that are aligned with reasonable cell designs for high specific energy RLBs. As shown in Figs. 3-6, distinct differences in cycle life emerge as the amount of electrolyte used in the Li || NMC622 cell approached the levels needed to attain a reasonable RLB cell. When the electrolyte quantity is reduced to the range needed to achieve a 240 Wh kg^{-1} design (6.0 g Ah^{-1}), the overall cycle life, to complete failure, drops by a factor of 6.5 (from 542 to 83 cycles).

Reducing electrolyte quantity also alters the failure pathway with two primary routes identified. First, in lean conditions, the failure is due to rapid electrolyte consumption. The second pathway, for excess electrolyte, is more involved with factors related to the positive electrode, kinetic limitations and loss of available Li.

The first of the failure pathways, for the lean electrolytes, is the rapid consumption of electrolyte. Supporting this pathway are several observations from the combined analysis of the charge and discharge portions of the dQ dV^{-1} plots (Fig. 7) and rate capability variation in Fig. 8. The lack of a significant shift prior to failure for the peaks associated with the NMC622 suggests that the failure has very little to do with the positive electrode. Additionally, the response of the negative electrode was not significantly impacted at a C/20 rate during cycling through the first two RPTs. At a C/3 rate, kinetic limitation was observed, but the decrease was less than for other electrolyte quantities with much longer cycle life, indicating material utilization was not the primary failure mode. Based on the extent of cycling for the higher electrolyte quantities, it is also evident that overall depletion of Li metal was not the major cause of failure. The lack of significant rate capability shift prior to failure further supports a rapid failure onset, likely due to consumption of electrolyte and subsequent inability to effectively shuttle Li^{+} ions between electrodes during charging and discharging. The rapid failure induced by the consumption of the lean electrolyte is also likely the key driver in the enhanced variability across the 6.0 and 10.2 g Ah^{-1} cells, where minor differences in the Li surface and evolution of the cells would have a more profound impact on performance.

The cells with higher electrolyte amounts, failed through a second pathway. For these electrolyte-rich cells, the failure involved aging of the positive electrode, electrode kinetics, and loss of accessible Li from the negative electrode. With respect to the positive electrode performance, the decreased intensity in the dQ dV^{-1} charging peaks (Fig. 7) between 3.6 and 3.75 V suggest that there was a slight loss in the accessible NMC622 positive electrode material. Additionally, the decreased slope during the initial portion of charging near 3.7 V and the less intense peak associated with the Li electrode kinetics suggest that kinetic factors started to impact the cycling performance even at a C/20 rate. Further evidence of electrode kinetics can be drawn from the discharge profiles in Figs. 5 and 6 for the 37.0 g Ah^{-1} condition where the lower slope and the distinct kink in RPT19 for both the C/3 and C/20 data has previously been attributed to transport limitations associated with complex Li metal morphology at the negative electrode [5,31]. The gradually decreasing ratio in C/3: C/20 capacity (Fig. 8) provides additional support for diminished electrode kinetics.

Combined, the slower electrode kinetics and the significant enhancement in cycle life for the 37.0 g Ah^{-1} condition suggest that decreased transport of Li^+ in the electrolyte was not the primary cause of failure as noted in the lean electrolyte cells. Rather, loss of accessible, electrochemically active Li from the negative electrode and decreased performance from the positive electrode become additional contributing factors as the electrolyte quantity increased. Unlike the first failure pathway, the use of excess electrolyte masks variations among a group of cells.

Using the volume of cell components and the internal dimensions of the cell, a total void of just over 200 μL is calculated. With this volume it is apparent that even when 75 μL of electrolyte are used there is still excess space remaining in the cell. Based on cell configuration the bulk of the excess cell volume is separated from the electrode stack and resides in the vicinity of the internal spring of the CR2032. This area has little access to the added electrolyte. As such, the bulk of the electrolyte is likely near the electrode stack. Given the close proximity it is possible that as the Li negative electrode is cycled and becomes more porous and tortuous that excess electrolyte replenishes consumed electrolyte within the electrode stack improving and extending performance. Thus, while a comparison between different electrolytes is feasible using flooded conditions, little information can be translated to a high specific energy cell design and possible key failure mechanisms or the importance of variability can be easily overlooked.

As with the low electrolyte quantity, the failure rate for both intermediate quantities was relatively rapid suggesting electrolyte depletion and failure. However, for the 12.0 g Ah^{-1} some of the key shifts in positive electrode capacity in the dQ dV^{-1} plots are observed, as is the decreased discharge profile slope indicative of kinetic limitations at the Li metal electrode. For these intermediate cases, electrolyte is still a key limiting factor, but the evolution of other aging modes such as electrode kinetics allows additional information to be gleaned from the analysis.

Conclusions

Through a combined design of experiment which was guided by an electrochemical model it has been shown that the use of lean electrolyte profoundly impacts cycle life and identification of failure modes for RLBs. Reducing the amount of electrolyte from 37.0 to 6.0 g Ah^{-1} decreased cycle life by a factor of 6.5. It also distinctly changed the cell failure mode. Two failure pathways are described here: first, in lean conditions, is rapid electrolyte consumption. Second, in flooded electrolyte conditions, is a more complex evolution associated with fade from electrolyte loss and incomplete utilization of both positive and negative electrodes. An intermediate path that entails both relatively rapid electrolyte consumption with kinetic variation at the negative electrode was also observed.

Combined the reduced cycle life and variation in failure mechanisms highlights the attention that needs to be paid to realistic experimental conditions when performing analysis on new materials and technologies for high energy RLB cell designs. The other key distinction which emerges as part of the present work is that as the quantity of electrolyte becomes closer to the levels needed to achieve a reasonably high specific energy cell, cell-to-cell variability increases.

Acknowledgements

Research has been supported by the Assistant Secretary for Energy Efficiency and Renewable Energy, Office of Vehicle Technologies of the U.S. Department of Energy through the Advanced Battery Materials Research (BMR) Program (Battery500 Consortium). INL is operated by Battelle Energy Alliance under Contract Nos. DE- DE-AC07-05ID14517 for the U.S. Department of Energy. PNNL is operated by Battelle for the U.S. Department of Energy under contract DE-AC05-76RLO1830. The author's would like to thank Bryant Polzin at Argonne National Laboratory, and Peter Faguy in the Vehicle Technologies Office of DOE-EERE for access to electrode laminate samples. The United States Government retains and the publisher, by accepting the article for publication, acknowledges that the United States Government retains a nonexclusive, paid-up, irrevocable, world-wide license to publish or reproduce the published form of this manuscript, or allow others to do so, for United States Government purposes.

References

[1] B. Nykvist, M. Nilsson, Rapidly falling costs of battery packs for electric vehicles, Nat. Clim Change. 5 (2015) 329–332.

[2] M.S. Whittingham, Ultimate Limits to Intercalation Reactions for Lithium Batteries, Chem. Rev. 114 (2014) 11414–11443. doi:10.1021/cr5003003.

[3] A. Manthiram, B. Song, W. Li, A perspective on nickel-rich layered oxide cathodes for lithium-ion batteries, Energy Storage Mater. 6 (2017) 125–139. doi:10.1016/j.ensm.2016.10.007.

[4] H.-J. Noh, S. Youn, C.S. Yoon, Y.-K. Sun, Comparison of the structural and electrochemical properties of layered Li[NixCoyMnz]O2 (x = 1/3, 0.5, 0.6, 0.7, 0.8 and 0.85) cathode material for lithium-ion batteries, J. Power Sources. 233 (2013) 121–130. doi:10.1016/j.jpowsour.2013.01.063.

[5] K.-H. Chen, K.N. Wood, E. Kazyak, W.S. LePage, A.L. Davis, A.J. Sanchez, N.P. Dasgupta, Dead lithium: mass transport effects on voltage, capacity, and failure of lithium metal anodes, J. Mater. Chem. A. 5 (2017) 11671–11681. doi:10.1039/C7TA00371D.

[6] X. Han, Y. Gong, K. (Kelvin) Fu, X. He, G.T. Hitz, J. Dai, A. Pearse, B. Liu, H. Wang, G. Rubloff, Y. Mo, V. Thangadurai, E.D. Wachsman, L. Hu, Negating interfacial impedance in garnet-based solid-state Li metal batteries, Nat. Mater. 16 (2016) 572.

[7] R. Hongahally Basappa, T. Ito, T. Morimura, R. Bekarevich, K. Mitsuishi, H. Yamada, Grain boundary modification to suppress lithium penetration through garnet-type solid electrolyte, J. Power Sources. 363 (2017) 145–152. doi:10.1016/j.jpowsour.2017.07.088.

[8] S.M. Choi, I.S. Kang, Y.-K. Sun, J.-H. Song, S.-M. Chung, D.-W. Kim, Cycling characteristics of lithium metal batteries assembled with a surface modified lithium

electrode, 16th Int. Meet. Lithium Batter. IMLB. 244 (2013) 363–368. doi:10.1016/j.jpowsour.2012.12.106.

[9] C. Yang, K. Fu, Y. Zhang, E. Hitz, L. Hu, Protected Lithium-Metal Anodes in Batteries: From Liquid to Solid, Adv. Mater. 29 (2017) 1701169–n/a. doi:10.1002/adma.201701169.

[10] X.-B. Cheng, R. Zhang, C.-Z. Zhao, Q. Zhang, Toward Safe Lithium Metal Anode in Rechargeable Batteries: A Review, Chem. Rev. 117 (2017) 10403–10473. doi:10.1021/acs.chemrev.7b00115.

[11] H. Xiang, P. Shi, P. Bhattacharya, X. Chen, D. Mei, M.E. Bowden, J. Zheng, J.-G. Zhang, /W. Xu, Enhanced charging capability of lithium metal batteries based on lithium bis(trifluoromethanesulfonyl)imide-lithium bis(oxalato)borate dual-salt electrolytes, J. Power Sources. 318 (2016) 170–177. doi:10.1016/j.jpowsour.2016.04.017.

[12] J. Zheng, M.H. Engelhard, D. Mei, S. Jiao, B.J. Polzin, J.-G. Zhang, W. Xu, Electrolyte additive enabled fast charging and stable cycling lithium metal batteries, Nat. Energy. 2 (2017) 17012.

[13] H. Xiang, P. Shi, P. Bhattacharya, X. Chen, D. Mei, M.E. Bowden, J. Zheng, J.-G. Zhang, W. Xu, Enhanced charging capability of lithium metal batteries based on lithium bis(trifluoromethanesulfonyl)imide-lithium bis(oxalato)borate dual-salt electrolytes, J. Power Sources. 318 (2016) 170–177. doi:10.1016/j.jpowsour.2016.04.017.

[14] S.M. Wood, C. Fang, E.J. Dufek, S.C. Nagpure, S.V. Sazhin, B. Liaw, Y.S. Meng, Predicting Calendar Aging in Lithium Metal Secondary Batteries: The Impacts of Solid Electrolyte Interphase Composition and Stability, Adv. Energy Mater. 0 (2018) 1801427. doi:10.1002/aenm.201801427.

[15] M.M. Thackeray, C. Wolverton, E.D. Isaacs, Electrical energy storage for transportation-approaching the limits of, and going beyond, lithium-ion batteries, Energy Env. Sci. 5 (2012) 7854–7863. doi:10.1039/C2EE21892E.

[16] T.R. Tanim, C.D. Rahn, C.-Y. Wang, A Temperature Dependent, Single Particle, Lithium Ion Cell Model Including Electrolyte Diffusion, J. Dyn. Syst. Meas. Control. 137 (2014) 011005-011005-11. doi:10.1115/1.4028154.

[17] T.R. Tanim, C.D. Rahn, Aging formula for lithium ion batteries with solid electrolyte interphase layer growth, J. Power Sources. 294 (2015) 239–247. doi:10.1016/j.jpowsour.2015.06.014.

[18] M.W. Verbrugge, B.J. Koch, Microelectrode investigation of ultrahigh-rate lithium deposition and stripping, J. Electroanal. Chem. 367 (1994) 123–129. doi:10.1016/0022-0728(93)03047-S.

[19] W.A. Appiah, J. Park, S. Song, S. Byun, M.-H. Ryou, Y.M. Lee, Design optimization of LiNi0.6Co0.2Mn0.2O2/graphite lithium-ion cells based on simulation and experimental data, J. Power Sources. 319 (2016) 147–158. doi:10.1016/j.jpowsour.2016.04.052.

[20] P. Arora, M. Doyle, R.E. White, Mathematical Modeling of the Lithium Deposition Overcharge Reaction in Lithium-Ion Batteries Using Carbon-Based Negative Electrodes, J. Electrochem. Soc. 146 (1999) 3543–3553. doi:10.1149/1.1392512.

[21] S. Cui, Y. Wei, T. Liu, W. Deng, Z. Hu, Y. Su, H. Li, M. Li, H. Guo, Y. Duan, W. Wang, M. Rao, J. Zheng, X. Wang, F. Pan, Optimized Temperature Effect of Li-Ion Diffusion with Layer Distance in Li(NixMnyCoz)O2 Cathode Materials for High Performance Li-Ion Battery, Adv. Energy Mater. 6 (2016) 1501309–n/a. doi:10.1002/aenm.201501309.

[22] L.O. Valøen, J.N. Reimers, Transport Properties of LiPF6-Based Li-Ion Battery Electrolytes, J. Electrochem. Soc. 152 (2005) A882–A891. doi:10.1149/1.1872737.

[23] M. Doyle, J. Newman, A.S. Gozdz, C.N. Schmutz, J. Tarascon, Comparison of Modeling Predictions with Experimental Data from Plastic Lithium Ion Cells, J. Electrochem. Soc. 143 (1996) 1890–1903. doi:10.1149/1.1836921.

[24] D. Lu, Y. Shao, T. Lozano, W.D. Bennett, G.L. Graff, B. Polzin, J. Zhang, M.H. Engelhard, N.T. Saenz, W.A. Henderson, P. Bhattacharya, J. Liu, J. Xiao, Failure Mechanism for Fast-Charged Lithium Metal Batteries with Liquid Electrolytes, Adv. Energy Mater. 5 (2015) 1400993–n/a. doi:10.1002/aenm.201400993.

[25] J. Qian, B.D. Adams, J. Zheng, W. Xu, W.A. Henderson, J. Wang, M.E. Bowden, S. Xu, J. Hu, J.-G. Zhang, Anode-Free Rechargeable Lithium Metal Batteries, Adv. Funct. Mater. 26 (2016) 7094–7102. doi:10.1002/adfm.201602353.

[26] X. Li, J. Zheng, X. Ren, M.H. Engelhard, W. Zhao, Q. Li, J.-G. Zhang, W. Xu, Dendrite-Free and Performance-Enhanced Lithium Metal Batteries through Optimizing Solvent Compositions and Adding Combinational Additives, Adv. Energy Mater. 8 (2018) 1703022. doi:10.1002/aenm.201703022.

[27] M. Dubarry, C. Truchot, B.Y. Liaw, Synthesize battery degradation modes via a diagnostic and prognostic model, J. Power Sources. 219 (2012) 204–216. doi:10.1016/j.jpowsour.2012.07.016.

[28] M. Dubarry, C. Truchot, M. Cugnet, B.Y. Liaw, K. Gering, S. Sazhin, D. Jamison, C. Michelbacher, Evaluation of commercial lithium-ion cells based on composite positive electrode for plug-in hybrid electric vehicle applications. Part I: Initial characterizations, J. Power Sources. 196 (2011) 10328–10335. doi:10.1016/j.jpowsour.2011.08.077.

[29] M. Dubarry, C. Truchot, B.Y. Liaw, K. Gering, S. Sazhin, D. Jamison, C. Michelbacher, Evaluation of commercial lithium-ion cells based on composite positive electrode for plug-in hybrid electric vehicle applications. Part II. Degradation mechanism under 2C cycle aging, J. Power Sources. 196 (2011) 10336–10343. doi:10.1016/j.jpowsour.2011.08.078.

[30] G. Bieker, M. Winter, P. Bieker, Electrochemical in situ investigations of SEI and dendrite formation on the lithium metal anode, Phys. Chem. Chem. Phys. 17 (2015) 8670–8679. doi:10.1039/C4CP05865H.

[31] K.N. Wood, E. Kazyak, A.F. Chadwick, K.-H. Chen, J.-G. Zhang, K. Thornton, N.P. Dasgupta, Dendrites and Pits: Untangling the Complex Behavior of Lithium Metal Anodes through Operando Video Microscopy, ACS Cent. Sci. 2 (2016) 790–801. doi:10.1021/acscentsci.6b00260.

[32] E.J. Dufek, J.R. Klaehn, J.S. McNally, H.W. Rollins, D.K. Jamison, Use of phosphoranimines to reduce organic carbonate content in Li-ion battery electrolytes, Electrochimica Acta. 209 (2016) 36–43. doi:10.1016/j.electacta.2016.05.038.

[33] M.K. Harrup, H.W. Rollins, D.K. Jamison, E.J. Dufek, K.L. Gering, T.A. Luther, Unsaturated phosphazenes as co-solvents for lithium-ion battery electrolytes, J. Power Sources. 278 (2015) 794–801. doi:10.1016/j.jpowsour.2014.07.109.

[34] H.W. Rollins, M.K. Harrup, E.J. Dufek, D.K. Jamison, S.V. Sazhin, K.L. Gering, D.L. Daubaras, Fluorinated phosphazene co-solvents for improved thermal and safety performance in lithium-ion battery electrolytes, J. Power Sources. 263 (2014) 66–74. doi:10.1016/j.jpowsour.2014.04.015.